Accelerating GW calculations with optimal polarizability basis

Feature Article

P. Umari[*,1], **X. Qian**[2], **N. Marzari**[2], **G. Stenuit**[1], **L. Giacomazzi**[1,3], and **S. Baroni**[1,3]

[1] CNR-IOM DEMOCRITOS Theory@Elettra Group, s.s. 14 km 163.5 in Area Science Park, 34149 Basovizza (Trieste), Italy
[2] Department of Materials Science and Engineering, MIT, 02139 Cambridge, MA, USA
[3] SISSA – Scuola Internazionale Superiore di Studi Avanzati, via Bonomea 265, 34126 Trieste, Italy

[*] Corresponding author: e-mail **pumari@sissa.it**, Phone: +39 040 3787 316, Fax: +39 040 3787 538

We present a method for accelerating GW quasi-particle (QP) calculations. This is achieved through the introduction of optimal basis sets for representing polarizability matrices. First the real-space products of Wannier like orbitals are constructed and then optimal basis sets are obtained through singular value decomposition. Our method is validated by calculating the vertical ionization energies of the benzene molecule and the band structure of crystalline silicon. Its potentialities are illustrated by calculating the QP spectrum of a model structure of vitreous silica. Finally, we apply our method for studying the electronic structure properties of a model of quasi-stoichiometric amorphous silicon nitride and of its point defects.

1 Introduction Density-functional theory (DFT) has grown into a powerful tool for the numerical simulation of matter at the nanoscale, allowing one to study the structure and dynamics of realistic models of materials consisting of up to a few thousands atoms, these days [1]. The scope of standard DFT, however, is limited to those dynamical processes that do not involve electronic excitations. Moreover, its time-dependent extension [2], which has been conceived to cope with such processes, still displays conceptual and practical difficulties.

The most elementary excitation is the removal or the addition of an electron from a system originally in its ground state. These processes are accessible to direct/inverse photoemission spectroscopies and can be described in terms of *quasi-particle* (QP) spectra [3]. In insulators, the energy difference between the lowest-lying quasi-electron state and the highest-lying quasi-hole state is the QP band gap, a quantity that is severely (and to some extent erratically) underestimated by DFT [4].

Many-body perturbation theory (MBPT), in turn, provides a general, though unwieldy, framework for calculating QP properties and other excitation (such as optical) spectra [3]. A numerically viable approach to QP energy (QPE) levels (known as the GW approximation, GWA) was introduced in the 1960s [5], but it took two decades for a realistic application of it to appear [6, 7], and even today the numerical effort required by MBPT is such that its scope is usually limited to systems of a few handfuls of inequivalent atoms. The two main difficulties are the necessity to calculate and manipulate large matrices representing the charge response of the system (electron polarizabilities or polarization propagators) [8], on the one hand, and that of expressing such response functions in terms of slowly converging sums over empty one-electron states [8, 9–11], on the other hand. Recently, we addressed both problems. In a first work [8] we introduced a method to significantly reduce the computational and memory loads of GWA calculations through the introduction of optimal basis sets for representing polarizability operators built upon Wannier-like orbitals [12–14]. Then, in a following communication [15], we proposed an approach to obtain fully converged GWA calculation avoiding at the same time any sum over empty states. In the same work we explained how also optimal polarizability basis sets can be constructed without explicitly evaluating empty states.

In this review, we present the strategy we have conceived for obtaining optimal polarizability basis sets and for calculating QPE levels, still considering sums over empty states. The paper is organized in this way: in Section 2 we briefly introduce the GW approximation, in Section 3 we describe our method for constructing optimal polarizability basis sets and for performing GWA calculations in isolated

and extended systems, in Section 4 we validate our method by considering the benzene molecule, crystalline silicon, and a model of vitreous silica, in Section 5 we use our method for studying the electronic properties of a model of quasi-stoichiometric amorphous silicon nitride and of its point defects. Conclusion and perspectives are drawn in Section 6.

2 The GW approximation QP energies and QP amplitudes (QPA) are eigenvalues and eigenvectors of a Schrödinger-like equation (QPEq), which is similar to the DFT Kohn–Sham equation with the exchange-correlation potential, $V_{xc}(\mathbf{r})$, replaced by the non-local, energy-dependent, and non-Hermitian self-energy operator, $\tilde{\Sigma}(\mathbf{r}, \mathbf{r}', E)$ (a tilde indicates the Fourier transform of a time-dependent function):

$$\left(-\frac{1}{2}\Delta + V_{ext} + \tilde{\Sigma}(E_n)\right)\xi_n = E_n\xi_n(\mathbf{r}), \qquad (1)$$

where we are using atomic units ($\hbar = 1$, $m = 1$, and $e = 1$) and V_{ext} is the external (ionic) potential and E_n and ξ_n are the n-th QPE and QPA, respectively. It is worth noting that the Hartree–Fock equation can be obtained from Eq. (1) by setting:

$$\tilde{\Sigma}(\mathbf{r}, \mathbf{r}'; E) = -\frac{\rho(\mathbf{r}, \mathbf{r}')}{|\mathbf{r}-\mathbf{r}'|}, \qquad (2)$$

where ρ is the one-particle density matrix and e is the elementary charge.

The next level of approximation is the GWA [5] where Σ is the product in time of the one-electron propagator, G, and of the dynamically screened interaction, W:

$$\Sigma_{GW}(\mathbf{r}, \mathbf{r}'; t) = iG(\mathbf{r}, \mathbf{r}'; t + \eta)W(\mathbf{r}, \mathbf{r}'; t), \qquad (3)$$

where η is a positive infinitesimal and W is expressed in terms of the bare Coulomb interaction $\upsilon(\mathbf{r}, \mathbf{r}')$ and of the reducible polarizability operator $\Pi(\mathbf{r}, \mathbf{r}'; t)$:

$$W = \upsilon + \upsilon \cdot \Pi \cdot \upsilon, \qquad (4)$$

where we indicate with a dot the product of two operators, such as in $\upsilon \cdot \chi(\mathbf{r}, \mathbf{r}', t) = \int d\mathbf{r}'' \upsilon(\mathbf{r}, \mathbf{r}'')\chi(\mathbf{r}'', \mathbf{r}'; t)$.

Then, the reducible polarizability operator is obtained from the irreducible polarizability operator P through the following Dyson's equation:

$$\Pi = (1-P \cdot \upsilon)^{-1} \cdot P. \qquad (5)$$

Finally, the irreducible polarizability is given from the product in time of one-electron propagators:

$$P(\mathbf{r}, \mathbf{r}'; t) = -iG(\mathbf{r}, \mathbf{r}'; t)G(\mathbf{r}', \mathbf{r}; -t). \qquad (6)$$

The GWA alone does not permit to solve the QPEq, unless G and W are known, possibly depending on the solution of the QPEq itself.

One of the most popular further approximations is the so-called $G^\circ W^\circ$ approximation, where the one-electron propagator G is obtained from the eigenfunctions $\psi_n(r)$ and eigenenergies ε_n of a one-electron (usually a Kohn–Sham) Hamiltonian:

$$\begin{aligned} G^\circ(\mathbf{r}, \mathbf{r}'; \tau) = &\ i\sum_\upsilon \psi_\upsilon(\mathbf{r})\psi_\upsilon^*(\mathbf{r})\, e^{-i\varepsilon_\upsilon\tau}\theta(-\tau) \\ &-i\sum_c \psi_c(\mathbf{r})\psi_c^*(\mathbf{r}')\, e^{-i\varepsilon_c\tau}\theta(\tau), \end{aligned} \qquad (7)$$

where, referred to the Fermi energy, υ and c suffixes indicate valence states below and conduction states above the Fermi energy, respectively, and θ is the Heaviside step function. Now, using the definition of G° in Eq. (6) is equivalent to calculating the irreducible polarizability within the random-phase approximation (RPA) which we indicate with P°. Then, from Eqs. (5) and (4), we obtain the approximate reducible polarizability operator Π° and dynamically screened Coulomb operator W°. Finally, the approximate self-energy operator in the $G^\circ W^\circ$ scheme is calculated through:

$$\Sigma_{G^\circ W^\circ}(\mathbf{r}, \mathbf{r}'; t) = iG^\circ(\mathbf{r}, \mathbf{r}'; t + \eta)W^\circ(\mathbf{r}, \mathbf{r}'; t). \qquad (8)$$

A further approximation, usually referred to as the diagonal approximation, is introduced for solving the QPEq: the QPAs are approximated directly with the non-interacting eigenfunctions:

$$\xi_n(\mathbf{r}) \approx \psi_n(\mathbf{r}). \qquad (9)$$

This permits to find the QPEs by solving the following self-consistent one-variable equation:

$$E_n \approx \varepsilon_n + \langle\tilde{\Sigma}_{G^\circ W^\circ}(E_n)\rangle_n - \langle V_{XC}\rangle_n, \qquad (10)$$

where $\langle A\rangle_n = \langle\psi_n|A|\psi_n\rangle$.

The apparently simple $G^\circ W^\circ$ approximation still involves severe difficulties, mainly related to the calculation and manipulation of the polarizability that enters the definition of W°. These difficulties are often addressed using the so-called plasmon-pole approximation [6], which however introduces noticeable ambiguities and inaccuracies when applied to inhomogeneous systems [16]. A well-established technique to address QP spectra in real materials without any crude approximations on response functions is the *space–time method* (STM) by Godby and coworkers [17]. In the STM the time/energy dependence of the $G^\circ W^\circ$ operators is represented on the imaginary axis, thus making them smooth (in the imaginary frequency domain) or exponentially decaying (in the imaginary time domain). The various operators are represented on a real-space grid, a choice which is straightforward, but impractical for systems larger than a few handfuls of inequivalent atoms. In the STM, the self-energy expectation value in Eq. (10) is obtained by analytically continuing to the real frequency axis the Fourier

transform of the expression:

$$
\langle \Sigma_{G^\circ W^\circ}(i\tau) \rangle_n = \mp \sum_l e^{\varepsilon_l \tau}
$$
$$
\times \int \psi_n(\mathbf{r})\psi_l(\mathbf{r})\psi_l(\mathbf{r}')\psi_n(\mathbf{r}')W^\circ(\mathbf{r},\mathbf{r}';i\tau)\,d\mathbf{r}\,d\mathbf{r}',
\tag{11}
$$

where the upper (lower) sign holds for positive (negative) times, the sum extends below (above) the Fermi energy, and QPAs are assumed to be real. For simplicity, in the rest of the paper, one-particle wavefunctions will be always considered to be real, which is always possible for time-symmetric systems. By substituting v for W, Eq. (11) yields the exchange self-energy, whereas $v \cdot \Pi \cdot v$ yields the correlation contribution, Σ_C, whose evaluation is the main size-limiting step of GW calculations.

3 The method: Optimal polarizability basis Let us suppose that a small, time-independent, orthonormal basis set $\{\Phi_\mu(\mathbf{r})\}$ exists for representing polarizability operators:

$$
\Pi(\mathbf{r},\mathbf{r}';i\tau) \approx \sum_{\mu\nu} \Pi_{\mu\nu}(i\tau)\Phi_\mu(\mathbf{r})\Phi_\nu(\mathbf{r}').
\tag{12}
$$

Then, the correlation contribution Σ_C to the self-energy is given by Eq. (11):

$$
\langle \Sigma_C(i\tau) \rangle_n \approx \mp \sum_{l\mu\nu} e^{\varepsilon_l \tau} \Pi_{\mu\nu}(i\tau) S_{nl,\mu} S_{nl,\nu} \theta(E_C^1 - \varepsilon_l),
\tag{13}
$$

where E_C^1 is an energy cutoff that limits the number of conduction states to be used in the calculation of the self-energy and:

$$
S_{nl,\nu} = \int \psi_n(\mathbf{r})\psi_l(\mathbf{r})\frac{1}{|\mathbf{r}-\mathbf{r}'|}\Phi_\nu(\mathbf{r}')\,d\mathbf{r}\,d\mathbf{r}'.
\tag{14}
$$

Then a convenient representation of the polarizability would thus allow QPEs to be calculated from Eq. (10), by analytically continuing to the real axis the Fourier transform of Eq. (13). Our goal is to shrink the dimension of the polarizability basis set $\{\Phi_\mu(\mathbf{r})\}$ without loss of accuracy. Therefore, an optimal polarizability basis would allow fast and accurate GW calculations.

We construct an optimal representation in three steps:

 (i) we first express the Kohn–Sham orbitals, whose products enter the definition of P°, in terms of localized, Wannier-like, orbitals,
 (ii) we then construct a basis set of localized functions for the manifold spanned by products of Wannier orbitals,
(iii) finally, this basis is further restricted to a set of approximate eigenvectors of P°, corresponding to eigenvalues larger than a given threshold.

Let us start from the RPA irreducible polarizability:

$$
\tilde{P}^\circ(\mathbf{r},\mathbf{r}';i\omega) = \sum_{cv} \overline{\Phi}_{cv}(\mathbf{r})\overline{\Phi}_{cv}(\mathbf{r}')\tilde{\chi}_{cv}^\circ(i\omega),
\tag{15}
$$

where

$$
\tilde{\chi}_{cv}^\circ(i\omega) = 2\mathrm{Re}\left(\frac{1}{i\omega - \varepsilon_c + \varepsilon_v}\right),
\tag{16}
$$

and

$$
\overline{\Phi}_{cv}(\mathbf{r}) = \psi_c(\mathbf{r})\psi_v(\mathbf{r}).
\tag{17}
$$

We express valence and conduction QPAs in terms of localized, orthonormal maximally localized Wannier functions [12, 14]:

$$
\begin{aligned}
u_s(\mathbf{r}) &= \sum_v \mathcal{U}_{vs}\psi_v(\mathbf{r})\theta(-\varepsilon_v)\\
v_s(\mathbf{r}) &= \sum_c \mathcal{V}_{cs}\psi_c(\mathbf{r})\theta(\varepsilon_c)\theta(E_C^2 - \varepsilon_c),
\end{aligned}
\tag{18}
$$

where $E_C^2 \le E_C^1$ is a second energy cutoff that limits a *lower conduction manifold* (LCM) to be used *only* in the construction of the polarizability basis and the $\mathcal{U}$ and $\mathcal{V}$ matrices are unitary.

We then reduce the number of product functions from the product, which scales quadratically with the system size, between the number of valence and the number of conduction states, to a number that scales linearly. Indeed, we have transformed the problem of calculating products in real space of delocalized (usually Kohn–Sham) orbitals in that of calculating products in real space of localized Wannier functions. We express the $\overline{\Phi}$'s as approximate linear combinations of products of the u's v's:

$$
\overline{\Phi}_{cv}(\mathbf{r}) \approx \sum_{rs} \mathcal{O}_{cv,rs} W_{rs}(\mathbf{r})\theta(|W_{rs}|^2 - s_1),
\tag{19}
$$

where:

$$
\mathcal{O}_{cv,c'v'} = \mathcal{U}_{vv'}\mathcal{V}_{cc'},
\tag{20}
$$

and the products in real space are given by:

$$
W_{rs}(\mathbf{r}) = u_r(\mathbf{r})v_s(\mathbf{r}),
\tag{21}
$$

and $|W_{cv}|$ is the L^2 norm of $W_{rs}(\mathbf{r})$, which is arbitrarily small when the centers of the u_r and v_s functions are sufficiently distant, and s_1 is an appropriate threshold.

The number of basis functions can be further reduced on account of the non-orthogonality of the W's. Indeed it is possible to obtain an orthonormal basis for representing the W's whose dimension can be significant smaller that the number of retained W's. This is done through a procedure analogous to a singular value decomposition. We first define the overlap matrix:

$$
\mathcal{Q}_{\rho\sigma} = \int W_\rho(\mathbf{r})W_\sigma(\mathbf{r})\,d\mathbf{r},
\tag{22}
$$

where the ρ and σ indices stand for pairs of rs indices. Then, we calculate the eigenvalues $\{q_\nu\}$ and eigenvectors $\{\mathcal{U}_\nu\}$ of the matrix $\mathcal{Q}$. It should be noted that the matrix $\mathcal{Q}$ is always positive definite. The magnitude of the eigenvalues is a measure of the relevance of their corresponding eigenvectors. Indeed an orthonormal basis sets which spans the space of the $\{W_\rho\}$ is given by the states Φ:

$$\Phi_\nu(\mathbf{r}) = \frac{1}{\sqrt{q_\nu}} \sum_\rho \mathcal{U}_{\nu\rho} W_\rho(\mathbf{r}). \tag{23}$$

An optimal polarizability basis can be obtained by retaining those Φ's for which q_ν is larger than a given threshold, s_2. We can now write:

$$\overline{\Phi}_{c\upsilon}(\mathbf{r}) \approx \sum_{\rho'\nu'} \mathcal{O}_{c\upsilon,\rho'} \sqrt{q_{\nu'}} \mathcal{U}_{\nu'\rho'}, \tag{24}$$

where the indices ρ' and ν' run only over the elements which have been retained according to the thresholds s_1 and s_2, respectively.

It is worth noting that the optimal polarizability basis vectors $\{\Phi_\nu\}$ are the (approximate) eigenvectors of the polarizability operator P' at zero time constructed with empty states only from the LCM:

$$P'(\mathbf{r}, \mathbf{r}) = \sum_{\upsilon c'} \overline{\Phi}_{\upsilon c'}(\mathbf{r}) \overline{\Phi}_{\upsilon c'}(\mathbf{r}'), \tag{25}$$

where c' indicates the empty states belonging to the LCM. As the $\mathcal{U}$ and $\mathcal{V}$ matrices are unitary, it holds:

$$P'(\mathbf{r}, \mathbf{r}) \approx \sum_{\rho'} W_{\rho'}(\mathbf{r}) W_{\rho'}(\mathbf{r}'). \tag{26}$$

From this equation and from Eq. (24), it is easy to show that:

$$\int d\mathbf{r}' P'(\mathbf{r}, \mathbf{r}) \Phi_\nu(\mathbf{r}') \approx q_\nu \Phi_\nu(\mathbf{r}). \tag{27}$$

This means that the construction of the polarizability basis selects the most important eigenvectors of the polarizability at least at zero time. We have verified, however, that the manifold spanned by the most important eigenvectors of P° in the (imaginary) time domain depends very little on time, which permits the use of a same basis at different frequencies. We have also verified that although the polarizability basis has been constructed only with empty states from the LCM, it behaves very well also for representing polarizability operators constructed with much more complete sets of empty states.

It should be noted that equivalent optimal polarizability basis sets could be constructed by choosing $s_1 = 0$ and by considering directly products of Kohn–Sham orbitals without transforming them into localized Wannier functions. Going through Wannier functions and discarding small overlaps permits only to speed up the construction of the polarizability basis set. Indeed, this results into a $O(N^3)$

process instead of a $O(N^4)$ process. This means that also for systems presenting delocalized orbitals it will always be possible to obtain optimal polarizabilty basis sets. However, in the limit case in which Kohn–Sham orbitals are simply plane waves, the optimal polarizability basis will be simply a basis of plane-waves. Hence, we expect to find larger benefits from the use of optimal polarizability basis sets in the case of isolated materials and in that of extended insulators, while in the limit of small gap extended systems we do not expect to find significant improvements with respect to the use of plane-waves basis sets.

Once an optimal basis set has been identified, an explicit representation for the irreducible polarizability,

$$\tilde{P}^\circ(\mathbf{r}, \mathbf{r}'; i\omega) = \sum_{\mu\nu} \tilde{P}^\circ_{\mu\nu}(i\omega) \Phi_\mu(\mathbf{r}) \Phi_\nu(\mathbf{r}'), \tag{28}$$

is obtained. By equating Eq. (15) to Eq. (28) and taking into account the orthonormality of the Φ's, one obtains:

$$\tilde{P}^\circ_{\nu\mu}(i\omega) = \sum_{c\upsilon} T_{c\upsilon,\mu} T_{c\upsilon,\nu} \tilde{\chi}^\circ_{c\upsilon}(i\omega) \theta(E_C^1 - \varepsilon_c), \tag{29}$$

with

$$T_{c\upsilon,\mu} = \int \overline{\Phi}_{c\upsilon}(\mathbf{r}) \Phi_\mu(\mathbf{r}) \, d\mathbf{r}, \tag{30}$$

where the index c runs over all the empty states defined by the cutoff E_C^1. Finally, a representation for Π is obtained by simple matrix manipulations.

While isolated system can be easily treated by applying in Eq. (14) a truncated form of the Coulomb potential [18], extended ones require some additional steps which we briefly introduce here. Note that in the present work the Brillouin zone is generally sampled at the Γ-point only. First, it is convenient to introduce the frequency dependent symmetric dielectric matrix [19]:

$$\tilde{\varepsilon}^{\mathrm{sym}}(i\omega) = 1 - \upsilon^{1/2} \cdot \tilde{P}^\circ(i\omega) \cdot \upsilon^{1/2}, \tag{31}$$

where υ is the Coulomb interaction. From $\varepsilon^{\mathrm{sym}}$ the screened Coulomb interaction W is given by:

$$\tilde{W}^\circ(i\omega) = \upsilon^{1/2} \cdot \tilde{\varepsilon}^{\mathrm{sym},-1}(i\omega) \cdot \upsilon^{1/2}. \tag{32}$$

Because of the long-range character of the Coulomb interaction, the long-wavelength components, the "head" ($\mathbf{G} = \mathbf{G}' = 0$) and "wings" ($\mathbf{G} = 0$, $\mathbf{G}' \neq 0$), of $\tilde{\varepsilon}^{\mathrm{sym}}(i\omega)$ cannot be neglected. As the optimal polarizability basis is orthogonal to the $\mathbf{G} = 0$ component, we calculate $\varepsilon^{\mathrm{sym}}(i\omega)$ on the representation of the optimal polarizability basis plus the $\mathbf{G} = 0$ vector. This is done by calculating the head and wings terms at frequency $i\omega$ using a linear response approach [20], where optionally the Brillouin zone can be sampled with denser meshes of k-points [21], and by projecting the wings over the polarizability basis functions. Then, we extract from

Phys. Status Solidi B **248**, No. 3 (2011)

531

Feature

Article

$\tilde{W}$ the long-range part behaving as υ:

$$\tilde{W}^{\circ}(i\omega) = \tilde{\varepsilon}^{\text{sym},-1}_{\mathbf{G}=0\mathbf{G}'=0}(i\omega)\upsilon$$
$$+ \sum_{\mu\nu} \upsilon^{1/2}|\Phi_\mu\rangle(\tilde{\varepsilon}^{\text{sym},-1}_{\mu\nu}(i\omega)-\delta_{\mu,\nu}\tilde{\varepsilon}^{\text{sym},-1}_{\mathbf{G}=0\mathbf{G}'=0}(i\omega))\langle\Phi_\nu|\upsilon^{1/2}.$$

$$(33)$$

The contribution to Σ_{C} due to the long-range part of W is then given by:

$$\langle\Sigma^{\text{lr}}_{\text{C}}(i\tau)\rangle_n \approx \sum_l \int d\mathbf{r}\, d\mathbf{r}' \frac{\psi_n(\mathbf{r})\psi_l(\mathbf{r})\psi_l(\mathbf{r}')\psi_n(\mathbf{r}')}{|\mathbf{r}-\mathbf{r}'|}$$
$$\times \left(\varepsilon^{\text{sym},-1}_{\mathbf{G}=0\mathbf{G}'=0}(i\tau)-1\right)e^{\varepsilon_l\tau}\theta(E^1_{\text{C}}-\varepsilon_l).$$

$$(34)$$

As the calculation of such terms closely resembles the evaluation of exchange terms, we calculate them using the scheme introduced in Ref. [22], optionally using a denser sampling of the BZ. Finally, the contribution to Σ_{C} due to the short-range part of W is given by:

$$\langle\Sigma^{\text{sr}}_{\text{C}}(i\tau)\rangle_n \approx \mp \sum_{l\nu'\mu\nu'} e^{\varepsilon_l\tau}S_{nl,\mu}S_{nl,\nu}\theta(E^1_C-\varepsilon_l)$$
$$\times \upsilon^{-1/2}_{\mu\mu'}\left(\varepsilon^{\text{sym},-1}_{\mu'\nu'}(i\tau)-\delta_{\mu',\nu'}\varepsilon^{\text{sym},-1}_{\mathbf{G}=0\mathbf{G}'=0}(i\tau)\right)\upsilon^{-1/2}_{\nu'\nu},$$

$$(35)$$

where the operator υ is calculated first on the polarizability basis:

$$\upsilon_{\mu\nu} = \langle\Phi_\mu|\upsilon|\Phi_\nu\rangle.$$

$$(36)$$

The evaluation of Eq. (36) does not present any difficulty as the polarizability basis functions Φ's are orthogonal to the $\mathbf{G}=0$ vector.

4 Implementation and validation Our scheme has been implemented in the QUANTUM-ESPRESSO density functional package [23], for norm-conserving as well as ultra-soft [24] pseudopotentials, resulting in a new module called *gww.x* which uses a Gauss–Legendre discretization of the imaginary time/frequencies half-axes, and that is parallelized accordingly. In the following examples, DFT calculations were performed using the energy functional from Ref. [25] and pseudo-potentials have been taken from the Quantum-Espresso tables [23]. We used an imaginary time cutoff of 10 a. u., an imaginary frequency cutoff of 20 Ry, and grids of 80 steps in both cases. The self-energy was analytically continued using a two poles formula [17].

4.1 Benzene We first illustrate our scheme by considering an isolated benzene molecule in a periodically repeated cubic cell with an edge of 20 a.u. using a first conduction energy cutoff $E^1_{\text{C}} = 56.7\,\text{eV}$, corresponding to 1000 conduction states, and a threshold on the norm of Wannier products $s_1 = 0.1$ a.u. We used the norm-conserving pseudopotentials: C.pz-vbc and H.pz-vbc. The wavefunctions and the charge density were expanded on plane waves, defined by kinetic energy cutoffs of 40 and 160 Ry,
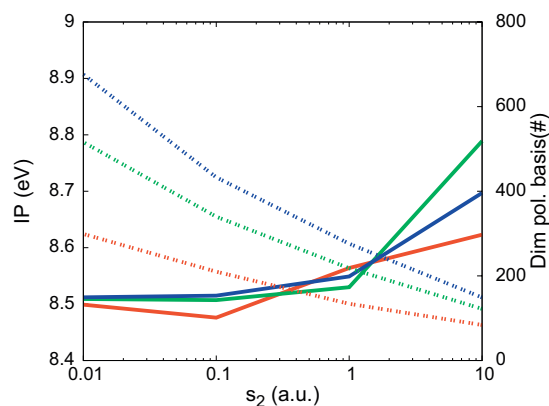
Figure 1 (online color at: www.pss-b.com) Calculated ionization potential of the benzene molecule (solid lines, left scale) and dimension of the polarization basis (dashed lines, right scale) *versus* the s_2 cutoff. The polarization basis has been constructed with a conduction energy cutoff $E^2_{\text{C}} = 16.7\,\text{eV}$ (red, 100 states), $E^2_{\text{C}} = 28.6\,\text{eV}$ (green, 300 states), and $E^2_{\text{C}} = 38.3\,\text{eV}$ (blue, 500 states).

respectively. In Fig. 1 we display the dependence of the calculated ionization potential (IP) on the second conduction energy cutoff used to define the polarization basis, E^2_{C}, and on the cutoff on the eigenvalues of the overlap matrix between Wannier products, s_2. Convergence within 0.01 eV is achieved with a conduction energy cutoff E^2_{C} smaller than 30 eV (less than 300 states) and a polarizability basis set of only $\sim$400 elements. The convergence of other QPEs is similar.

In Fig. 2, we display the convergence of the IP with respect to E^1_{C}, which turns out to be quite slow. These data can be accurately fitted by the simple formula:

$$\text{IP}(E^1_{\text{C}}) = \text{IP}(\infty) + \frac{A}{E^1_{\text{C}}},$$

$$(37)$$

resulting in a predicted ionization potential $\text{IP}(\infty) = 9.1\,\text{eV}$, in good agreement with the experimental value of 9.3 eV [26].
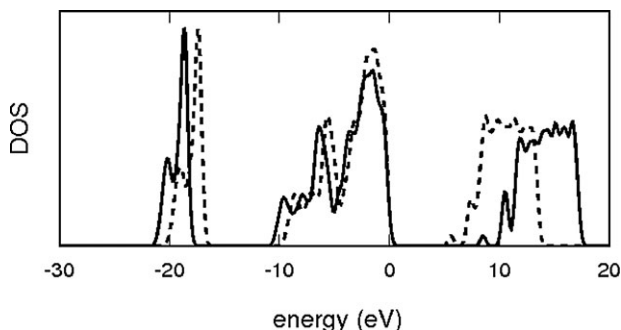
4.2 Bulk Si In order to demonstrate our scheme for extended systems, we consider crystalline silicon treated using a 64-atom simple cubic cell at the experimental lattice constant and sampling the corresponding Brillouin zone (BZ) using the Γ-point only. This gives the same sampling of the electronic states as would result from six points in the irreducible wedge of the BZ of the elementary 2-atom unit cell. We used an norm-conserving pseudopotential: Si.pz-rrkj. The wavefunctions and the charge density were expanded on plane waves, defined by kinetic energy cutoffs of 18 and 72 Ry, respectively. Then, the GW calculations were performed using $E^1_{\text{C}} = 94.6\,\text{eV}$ (corresponding to 3200 conduction states) and $E^2_{\text{C}} = 33.8\,\text{eV}$ (corresponding to 800 states in the LCM), $s_1 = 1.0$ a.u. and two distinct values for s_2 (0.01 and 0.001). For calculating the head and wing terms of
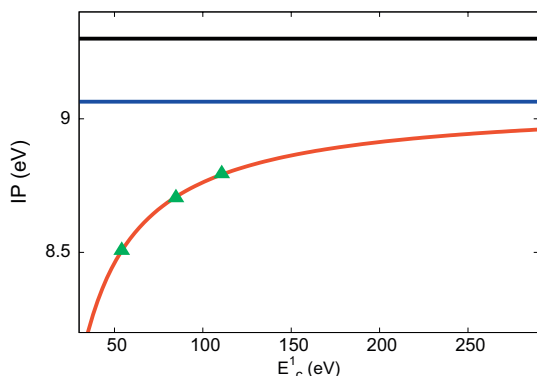
Figure 2 (online color at: www.pss-b.com) Calculated ionization potential as a function of the overall conduction energy cutoff, E_C^1. Black line: experimental value; red line: fit to the calculated values (green triangles); blue line extrapolated value. See text for more details.

Figure 3 Electronic density of states for a model of vitreous silica: LDA (dashed line) and GW (solid line). A Gaussian broadening of 0.25 eV has been used. The top of the valence band has been aligned to 0 eV.

the symmetric dielectric matrix we used a $4 \times 4 \times 4$ grid for sampling the BZ of the 64-atom cubic cell. Then, for calculating the long-range contribution to the self-energy given in Eq. (34), we used a $2 \times 2 \times 2$ grid. In Table 1 we summarize our results and compare them with previous theoretical results, as well as with experiments. An overall convergence within a few tens meV is achieved with a s_2 cutoff of 0.001 a.u., corresponding to a polarizability basis of $\sim$6500 elements. The residual small discrepancy with respect to previous results [17] is likely due to our use of a supercell, rather than the more accurate k-point sampling used in previous works.

4.3 Vitreous silica Our ability to treat large super-cells give us the possibility to deal with disordered systems that could hardly be addressed using conventional approaches. In Fig. 3 we show the QPE density of states (DOS) as calculated for a 72-atom model of vitreous silica [27].We used a norm-conserving for pseudopotential for Si (Si.pz-vbc) and an ultrasoft [24] one (O.pz-rrkjus) for O. The wavefunctions and the charge density were expanded on

Table 1 QPEs (eV) calculated in crystalline silicon and compared with experimental (as quoted in Ref. [17]) and previous theoretical results [17].

	Th$_1$	Th$_2$	prev th	expt
N_P	4847	6510		
Γ_{1v}	-11.45	-11.49	-11.57	-12.5 ± 0.6
X_{1v}	-7.56	-7.58	-7.67	
X_{4v}	-2.79	-2.80	-2.80	$-2.9, -3.3 \pm 0.2$
Γ'_{25c}	0.	0.	0.	0.
X_{1c}	1.39	1.41	1.34	1.25
Γ'_{15c}	3.22	3.24	3.24	3.40, 3.05
Γ'_{2c}	3.87	3.89	3.94	4.23, 4.1

"Th$_1$" and "Th$_2$" indicate calculations made with $s_2 = 0.01$ and $s_2 = 0.001$ a.u., respectively, while N_P is the dimension of the polarization basis.

plane waves, defined by kinetic energy cutoffs of 24 and 200 Ry, respectively. We used $E_C^1 = 48.8$ eV (corresponding to 1000 conduction states), $E_C^2 = 30.2$ eV (corresponding to 500 states in the LCM), $s_1 = 1$ a.u. and $s_2 = 0.1$ a.u. (giving rise to a polarization basis of 3152 elements). We checked the convergence with respect to the polarization basis by considering $s_2 = 0.01$ a.u. which leads to a basis of 3933 elements. Indeed, the calculated QPEs differ in average by only 0.01, eV with a maximum discrepancy of 0.07 eV. The QP band-gap resulting from our calculations is 8.5 eV, to be compared with an experimental value of $\sim$9 eV [28] and with a significantly lower value predicted by DFT in the local-density approximation (5.6 eV).

5 Example: Point defects in a-Si$_3$N$_4$ Amorphous silicon nitride (a-Si$_3$N$_4$) is being widely studied as its mechanical and electronic properties lead to a wide range of applications [29] In microelectronics, amorphous silicon nitride (a-Si$_3$N$_4$) is used to fabricate insulating layers in triple oxide-nitride-oxide structures [30]. In particular, because of its high concentration of charge traps, a-Si$_3$N$_4$ is employed as charge storage layer in non-volatile memory devices [31]. Moreover, silicon nitride based materials are nowadays proposed for optoelectronic devices [32]. Due to the non-trivial nature of its structures, first-principles methods become very important for investigating its properties at the atomistic scale [33]. We review here how our *gww* method permitted to investigate the electronic structure of quasi-stoichiometric a-Si$_3$N$_4$ addressing a 152-atoms model structure [33].

5.1 Model generation In a-Si$_3$N$_4$ silicon atoms are fourfold coordinated forming almost regular SiN$_4$ tetrahedra. The latter are connected by corners in such a way that each N atom is shared by three tetrahedra. Nitrogen atoms are threefold coordinated, with the silicon neighbors arranged at the vertexes of a planar triangle. This results in a quite rigid network structure. Furthermore the a-Si$_3$N$_4$ network is supposed to contain not only corner-sharing but also edge-sharing SiN$_4$ tetrahedra [33, 34].

Phys. Status Solidi B **248**, No. 3 (2011)

533

We generated a model of a-Si_3N_4 through first-principles molecular dynamics using the DFT approach and the exchange and correlation functional of Ref. [25]. Core-valence interactions were described through ultrasoft pseudopotentials [24] for N and H atoms and through a normconserving pseudopotential for Si atoms. The electronic wavefunctions and the charge density were expanded using plane waves basis sets defined by energy cutoffs of 25 and 200 Ry, respectively. The Brillouin's zone was sampled at the Γ-point. The model structure was generated through first-principles molecular dynamics starting from a diamond-cubic model of crystalline silicon which was changed into Si_3N_4 by addition of N atoms at intermediate distances between Si–Si neighbors. The initial model structure contained 64 Si and 86 N atoms in a periodically repeated cubic cell. A composition ratio $r = $ [N]/[Si] of 1.34 was chosen slightly differing from the ideal stoichiometry in order to trigger the formation of defects. We set up the density to the experimental value of 3.1 g/cm^3 [35]. Car and Parrinello [36] molecular dynamics runs were then performed for obtaining the model of a-Si_3N_4. First the system was thermalized at the temperature of 3500 K for 12 ps using a Nosé–Hoover thermostat [37]. Successively, the sample was quenched for 5 ps down to 2000 K below the theoretical melting point. Finally, the structural geometry was further optimized by a damped molecular dynamics run. As the model presented an empty state close to the top of the valence band, we passivated it by adding to the structure two H atoms in proximity of the two Si atoms which were threefold coordinated [38]. After structural relaxation, the H atoms moved close to two near N sites. We note that the structural and electronic properties of our model were only marginally affected by the addition of the two H atoms.

5.2 Model structure We report a picture of the final model structure in Fig. 4. The main structural parameters are reported in Table 2. The average Si–N bond length equals to 1.730 Å with a standard deviation (std) of 0.060 Å. This value is found to be in excellent agreement with the experimental bond length of 1.729 Å [39]. The structure shows well-defined SiN$_4$ tetrahedral units. The average N–Si–N angle equals 109.1° with a standard deviation of 13°. This is very close to the ideal angle of 109.47° for regular tetrahedra. Moreover our structure shows also well-defined quasi-planar NSi$_3$ units. The average Si–N–Si angle equals 117.2° with a standard deviation of 15°. This is consistent with the value of 120° for regular planar NSi$_3$ units.

The amount of SiN$_4$ tetrahedra and NSi$_3$ triangular units is reported in Table 3 where we give the coordination numbers in the first-neighbor shells of Si and N atoms, together with the relative Si–N bond length averages. The majority of Si atoms is fourfold coordinated and shows an average Si–N bond length of 1.73 Å. Few Si atoms are three- or fivefold coordinated. Correspondingly, almost all nitrogen atoms are bound to three silicon atoms and only a few show two- or fourfold coordination. Consequently, our model shows at short-range high topologic and chemical order. We
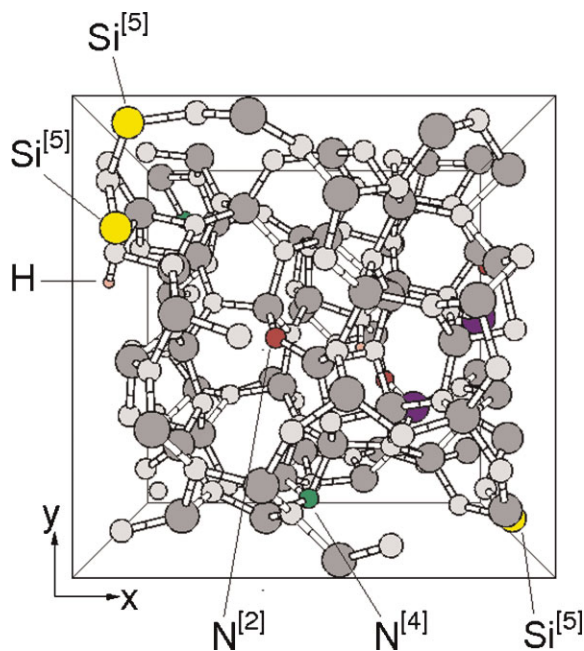
Figure 4 (online color at: www.pss-b.com) Balls-and-sticks picture of the a-Si_3N_4 model. Si atoms and N atoms are colored with dark and light gray, respectively. Threefold and fivefold coordinated Si atoms are colored in purple and yellow, respectively. Twofold and fourfold coordinated N atoms are colored in red and green. Hydrogen are colored in pink.

Table 2 Structural properties of our model of a-Si_3N_4 and reference values: average Si–N–Si and N–Si–N angles, and average bond length d_{SiN}.

	∠ Si–N–Si	∠ N–Si–N	d_{SiN} (Å)
model	117.2° (15.1°)	109.1° (13.0°)	1.73 (0.06)
ref.	120°^{a}	109.47°^{a}	1.729^b

The respective standard deviations are given in parenthesis.
^{a}Ideal bonding geometry. ^{b}Expt. (Ref. [39]).

Table 3 Composition of first-neighbor shells in our model of a-Si_3N_4.

composition	n_{Si}	d_{SiN}
Si[3]	2	1.64 (0.05)
Si[4]	59	1.73 (0.05)
Si[5]	3	1.81 (0.09)

| composition	n_N	d_{SiN}
N[2]	3	1.61 (0.03)
N[3]	79	1.73 (0.05)
N[4]	2	1.85 (0.09)
NSi$_3$H	2	1.78 (0.02)

Coordination numbers of Si and N atoms are indicated by the superscript number in square brackets. The number of Si and N atoms found in our model for each coordination are indicated by n_{Si} and n_N. Average Si–N bond length d_{SiN} (Å) together with its standard deviation (in parenthesis) is given for each composition. We used cutoff radii of 2.2 Å.

want now to understand the role of the point defects on the electronic structure.

5.3 Electronic structure For obtaining the polarizability basis we used a cutoff $E_C^2 = 30$ eV, corresponding to 750 empty states in the LCM, and thresholds $s_1 = 2$. a.u. and $s_2 = 0.1$. This gave rise to a polarization basis of 5867 elements. Then for the obtaining the self-energy we chose a cutoff $E_C^1 = 45$ eV, corresponding to 1500 empty states.

We show in Fig. 5a the electronic DOS for our model calculated with the GW approach together with the partial densities of s and p states for the Si and N atoms. The lowest part of the valence band mainly arises from N 2s states. While the low-energy side of the upper part of the valence band results from the Si–N bonds, formed by Si sp^3 and N 2p orbitals, the high-energy side, which defines the top of the valence band, consists of N 2p lone pairs. The low-energy side of the conduction band mainly consists of antibonding states associated to the Si–N bond. We note that the origin of the bands is analogous to the cases of SiO$_2$ (Ref. [40]) and GeO$_2$ (Ref. [41]), reflecting the common type of short-range arrangement of atoms based on the tetrahedral unit. Similar conclusions were obtained for the electronic DOS calculated through an approximate density-functional Scheme [42] and through a tight binding approach [43]. Moreover, the calculated valence band is consistent with photoemission spectra [44].

We focus now on the role played by the defects in the DOS. In Fig. 6a we give the partial DOS obtained by
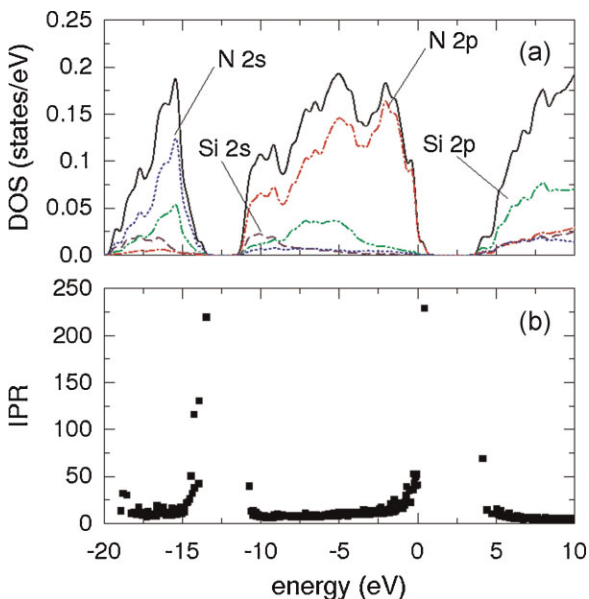
Figure 5 (online color at: www.pss-b.com) (a) Electronic density of states (black) and partial DOS obtained by projecting electronic states onto N 2s (blue/dotted), N 2p (red/dot-dashed), Si 2s (purple/dashed), and Si 2p (green/double dot-dashed). The highest occupied state is aligned at 0 eV. Gaussian broadening of 0.25 eV is used. GW energies are used. (b) Inverse participation ratio (IPR) of electronic states in silicon nitride.
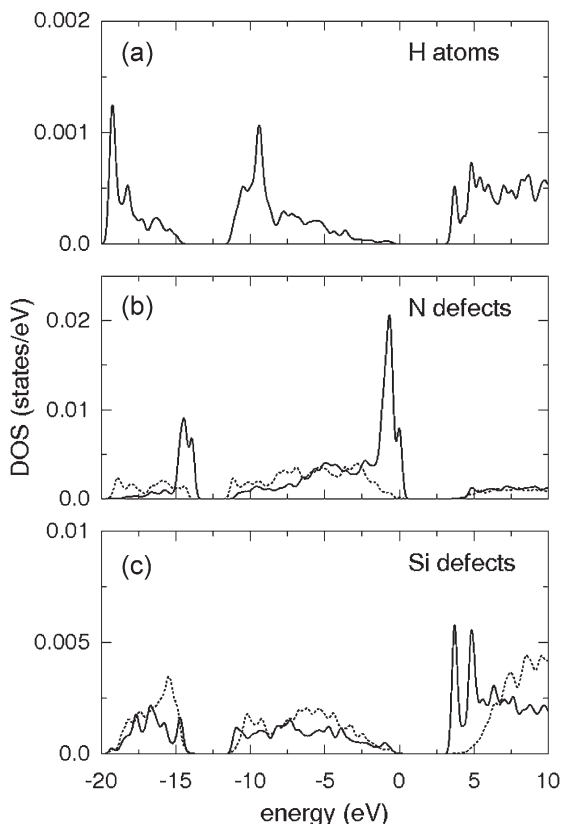
Figure 6 Partial DOS obtained by projecting the electronic states onto (a) 1s orbitals of H atoms, (b) 2p and 2s orbitals of twofold (solid) and fourfold (dotted) coordinated N atoms, (c) 2p and 2s orbitals of threefold (solid) and fivefold (dotted) coordinated Si atoms. The highest occupied state is aligned at 0 eV. Gaussian broadening of 0.25 eV is used. GW energies are used.

projecting the electronic states onto the 1s orbitals of the two H atoms of our model structure. The partial DOS of H atoms constitutes a very small contribution to the total DOS of Fig. 5. In Fig. 6b and c we show the partial DOS obtained by projecting the electronic states onto the 2p and 2s orbitals of the N[2] and N[4] atoms and of the Si[3] and Si[5] atoms. The partial DOS of N[4] atoms and Si[5] atoms do not show features localized near the band edges. At variance, the partial DOS of the N[2] atoms shows a sharp peak at the top of the valence band, while the partial DOS of Si[3] atoms exhibits sharp peaks close to the bottom of the conduction band [45]. As Fig. 6a illustrates, these peaks are originated by N and Si 2p orbitals of N[2] and Si[3] atoms, respectively. Furthermore, the topmost occupied electronic state and the first empty electronic state are spatially localized around a N[2] atom and around a Si[3] atom, respectively. By excluding these two defect states, we found a HOMO–LUMO band gap of 4.42 eV in excellent agreement with the experimental value of 4.55 eV of the optical band gap of sputtered a-Si$_3$N$_4$ given in Ref. [46]. However, we note that the band gap is quite sensitive to the adopted production method and for CVD samples is about 5.3 eV [46]. Yet, the GW method

appears to correctly describe the electronic DOS where simpler LDA calculations fail giving for our model structure a HOMO–LUMO band-gap of only 2.9 eV, as typical for LDA calculations in silicon nitride [38, 42].

We now analyze the degree of localization of the electronic states. The localization of an electronic state ψ_n can be quantified by the inverse participation ratio (IPR) [38, 47]:

$$\mathrm{IPR}_n = \Omega \frac{\int d\mathbf{r} |\psi_n(\mathbf{r})|^4}{\left|\int d\mathbf{r} |\psi_n(\mathbf{r})|^2\right|^2}, \tag{38}$$

where Ω is the volume of the simulation cell. The larger the IPR the more localized is the electronic state, so that highly localized/delocalized states show a large/small IPR. For completely delocalized states the IPR is equal to unity. In Fig. 5b we show the IPR for the electronic states of our model of silicon nitride. We note that the states close to the band edges corresponding to N[2] and Si[3] defects result much more localized than the other electronic states. These results are consistent with the IPR data previously calculated for a-SiN$_x$ in Ref. [38].

6 Conclusions We have shown how the use of optimal basis sets for representing the polarizability operator permits to achieve a significant speed up of GW calculations, allowing the study of large model structures up to a few hundreds of atoms. Therefore it is appealing to use such scheme for investigating the electronic structure of defects as density-functional approaches result not to be adequate. The main limitation still present in our approach is the need of summing over a large number of empty states. For a discussion of this point and the presentation of a solution we indicate to the reader Ref. [15].

References

[1] See e.g., R. M. Martin, Electronic Structure (Cambridge University Press, Cambridge, 2004) and references quoted therein.

[2] E. Runge and E. K. U. Gross, Phys. Rev. Lett. **52**, 997 (1984). M. A. L. Marques, C. L. Ullrich, F. Nogueira, A. Rubio, K. Burke, and E. K. U. Gross, Time-Dependent Density Functional Theory, Lecture Notes in Physics, Vol. 706 (Springer-Verlag, Berlin, Heidelberg, 2006).

[3] L. Hedin and S. Lundqvist, Solid State Phys. **23**, 1 (1969).

[4] F. Aryasetiawan and O. Gunnarsson, Rep. Prog. Phys. **61**, 237 (1998).

[5] L. Hedin, Phys. Rev. **139**, 796 (1965).

[6] M. S. Hybertsen and S. G. Louie, Phys. Rev. Lett. **55**, 1418 (1985).

[7] G. Onida, L. Reining, and A. Rubio, Rev. Mod. Phys. **74**, 601 (2001).

[8] P. Umari, G. Stenuit, and S. Baroni, Phys. Rev. B **78**, 201104 (2009).

[9] L. Reining, G. Onida, and R. W. Godby, Phys. Rev. B **56**, R4301 (1997).

[10] L. Steinbeck, A. Rubio, L. Reining, M. Torrent, I. D. Whited, and R. W. Godby, Comput. Phys. Commun. **125**, 105 (2000).

[11] F. Bruneval and X. Gonze, Phys. Rev. B **78**, 085125 (2008).

[12] N. Marzari and D. Vanderbilt, Phys. Rev. B **56**, 12847 (1997).

[13] I. Souza, N. Marzari, and D. Vanderbilt, Phys. Rev. B **65**, 035109 (2001).

[14] F. Gygi, J.-L. Fattebert, and E. Schwegler, Comput. Phys. Commun. **155**, 1 (2003).

[15] P. Umari, G. Stenuit, and S. Baroni, Phys. Rev. B **81**, 115104 (2010).

[16] R. Shaltaf, G.-M. Rignanese, X. Gonze, F. Giustino, and A. Pasquarello, Phys. Rev. Lett. **100**, 186401 (2008).

[17] H. N. Rojas, R. W. Godby, and R. J. Needs, Phys. Rev. Lett. **74**, 1827 (1995). M. M. Rieger, L. Steinbeck, I. D. White, H. N. Rojas, R. W. Godby, Comput. Phys. Commun. **117**, 211 (1999).

[18] G. Onida, L. Reining, R. W. Godby, R. Del Sole, and W. Andreoni, Phys. Rev. Lett. **75**, 818 (1995).

[19] S. Baroni and R. Resta, Phys. Rev. B **33**, 7017 (1986).

[20] S. Baroni, P. Giannozzi, and A. Testa, Phys. Rev. Lett. **58**, 1861 (1987).

[21] P. Umari and A. Pasquarello, Phys. Rev. B **68**, 085114 (2003).

[22] J. Spencer and A. Alavi, Phys. Rev. B **77**, 193110 (2008).

[23] P. Giannozzi, S. Baroni, N. Bonini, M. Calandra, R. Car, C. Cavazzoni, D. Ceresoli, G. L. Chiarotti, M. Cococcioni, I. Dabo, A. Dal Corso, S. de Gironcoli, S. Fabris, G. Fratesi, R. Gebauer, U. Gerstmann, C. Gougoussis, A. Kokalj, M. Lazzeri, L. Martin-Samos, N. Marzari, F. Mauri, R. Mazzarello, S. Paolini, A. Pasquarello, L. Paulatto, C. Sbraccia, S. Scandolo, G. Sclauzero, A. P. Seitsonen, A. Smogunov, P. Umari, and R. M. Wentzcovitch, J. Phys.: Condens. Matter **21**, 395502 (2009).

[24] D. Vanderbilt, Phys. Rev. B **41**, 7892 (1990).

[25] J. P. Perdew and A. Zunger, Phys. Rev. B **23**, 5048 (1981).

[26] N. O. Lipari, C. B. Duke, and L. Pietronero, J. Chem. Phys. **65**, 1165 (1976).

[27] J. Sarnthein, A. Pasquarello, and R. Car, Phys. Rev. Lett. **74**, 4682 (1995); Phys. Rev. B **52**, 12690 (1995).

[28] F. J. Himpsel, Surf. Sci. **168**, 764 (1986). F. J. Grunthaner and P. J. Grunthaner, Mater. Sci. Rep. **1**, 65 (1986).

[29] R. N. Katz, Science **208**, 841 (1980). A. Y. Liu, M. L. Cohen, Phys. Rev. B **41**, 10727 (1990).

[30] Y. Ma, T. Yasuda, and G. Lucovsky, Appl. Phys. Lett. **64**, 2226 (1994).

[31] H. Aozasa, I. F. Ujiwara, A. Nakamura, and Y. Komatsu, Jpn. J. Appl. Phys. **38**, 1441 (1999). H. Bachhofer, H. Reisinger, E. Bertagnolli, and H. von Philipsborn, J. Appl. Phys. **89**, 2791 (2001).

[32] L. Dal Negro, S. Hamel, N. Zaitseva, J. H. Yi, A. Williamson, M. Stolfi, J. Michel, G. Galli, and L. C. Kimerling, IEEE J. Sel. Top. Quantum Electron. **12**, 1151 (2006). L. Dal Negro, J. H. Yi, J. Michel, L. C. Kimerling, S. Hamel, A. Williamson, G. Galli, IEEE J. Sel. Top. Quantum Electon. **12**, 1628 (2006).

L. Dal Negro, J. H. Yi, L. C. Kimerling, S. Hamel, A. Williamson, G. Galli, Appl. Phys. Lett. **88**, 183103 (2006).

[33] L. Giacomazzi and P. Umari, Phys. Rev. B **80**, 144201 (2009).

[34] P. Kroll, J. Non-Cryst. Solids **293–295**, 238 (2001).

[35] S. M. Sze, Physics of Semiconductor Devices (John Wiley & Sons, Inc., New York, 1981).

[36] R. Car and M. Parrinello, Phys. Rev. Lett. **55**, 2471 (1985).

[37] S. Nosé, Mol. Phys. **52**, 255 (1984).
W. G. Hoover, Phys. Rev. A **31**, 1965 (1985).

[38] J. F. Justo, F. de BritoMota, and A. Fazzio, Phys. Rev. B **65**, 073202 (2002).
F. de Brito Mota, J. F. Justo, A. Fazzio, Braz. J. Phys. **32**, 436 (2002).

[39] M. Misawa, T. Fukunaga, K. Niihara, T. Hirai, and K. Suzuki, J. Non-Cryst. Solids **34**, 313 (1979).

[40] N. Binggeli, N. Troullier, J. L. Martins, and J. R. Chelikowsky, Phys. Rev. B **44**, 4771 (1991).
F. Giustino, A. Pasquarello, Phys. Rev. Lett. **96**, 216403 (2006).

[41] L. Giacomazzi, P. Umari, and A. Pasquarello, Phys. Rev. B **74**, 155208 (2006).

[42] F. Alvarez and A. A. Valladares, Rev. Mex. Fís. **48**, 528 (2002).

[43] A. N. Sorokin, A. A. Karpushin, V. A. Gritsenko, and H. Wong, J. Non-Cryst. Solids **354**, 1531 (2008).

[44] R. Kärcher, L. Ley, and R. L. Johnson, Phys. Rev. B **30**, 1896 (1984).

[45] L. Martn-Moreno, E. Martnez, J. A. Vergés, and F. Yndurain, Phys. Rev. B **35**, 9683 (1987).
S.-Y. Lin, Opt. Mater. **23**, 93 (2003).

[46] J. Bauer, Phys. Status Solidi **39**, 411 (1977).

[47] S. R. Elliott, Physics of Amorphous Materials (Longman, New York, 1984), p. 194.